Journal of Biomedical Optics

BiomedicalOptics.SPIEDigitalLibrary.org

Correcting spherical aberrations in a biospecimen using a transmissive liquid crystal device in two-photon excitation laser scanning microscopy

Ayano Tanabe
Terumasa Hibi
Sari Ipponjima
Kenji Matsumoto
Masafumi Yokoyama
Makoto Kurihara
Nobuyuki Hashimoto
Tomomi Nemoto

SPIE.

Correcting spherical aberrations in a biospecimen using a transmissive liquid crystal device in two-photon excitation laser scanning microscopy

Ayano Tanabe,[a,b,c] Terumasa Hibi,[a,b] Sari Ipponjima,[a,b] Kenji Matsumoto,[c] Masafumi Yokoyama,[c] Makoto Kurihara,[c] Nobuyuki Hashimoto,[c] and Tomomi Nemoto[a,b,*]
[a]Hokkaido University, Research Institute for Electronic Science, N20W10, Kita-Ward, Sapporo, Hokkaido 001-0020, Japan
[b]Hokkaido University, Graduate School of Information Science and Technology, N14W9, Kita-Ward, Sapporo, Hokkaido 060-0814, Japan
[c]Citizen Holdings Co. Ltd., 840, Shimotomi, Tokorozawa, Saitama 359-8511, Japan

Abstract. Two-photon excitation laser scanning microscopy has enabled the visualization of deep regions in a biospecimen. However, refractive-index mismatches in the optical path cause spherical aberrations that degrade spatial resolution and the fluorescence signal, especially during observation at deeper regions. Recently, we developed transmissive liquid-crystal devices for correcting spherical aberration without changing the basic design of the optical path in a conventional laser scanning microscope. In this study, the device was inserted in front of the objective lens and supplied with the appropriate voltage according to the observation depth. First, we evaluated the device by observing fluorescent beads in single- and two-photon excitation laser scanning microscopes. Using a 25× water-immersion objective lens with a numerical aperture of 1.1 and a sample with a refractive index of 1.38, the device recovered the spatial resolution and the fluorescence signal degraded within a depth of ±0.6 mm. Finally, we implemented the device for observation of a mouse brain slice in a two-photon excitation laser scanning microscope. An optical clearing reagent with a refractive index of 1.42 rendered the fixed mouse brain transparent. The device improved the spatial resolution and the yellow fluorescent protein signal within a depth of 0–0.54 mm. [DOI: 10.1117/1.JBO.20.10.101204]

Keywords: adaptive optics; liquid crystals; phase modulation; scanning microscopy; aberrations.

Paper 150089SSPR received Feb. 15, 2015; accepted for publication May 18, 2015; published online Aug. 5, 2015.

1 Introduction

Fluorescent proteins[1] have enabled us to observe cell shapes and the localization of molecules within live cells and tissue of transgenic animals expressing fluorescent protein, such as transgenic mice expressing green fluorescent protein. In the case of two-photon laser scanning microscopy (TPLSM), fluorescent molecules are excited within a small area around the focus.[2] This localization in the two-photon excitation process allows cross-sectional fluorescent imaging in the absence of a confocal aperture. In addition, near-infrared laser light used for two-photon excitation processes is negligibly absorbed or scattered in a biospecimen. Owing to these advantages, the use of fluorescent proteins and TPLSM has enabled us to three-dimensionally visualize deep regions within a biospecimen, such as the brain of a living mouse expressing fluorescent proteins.[3–6] On the other hand, several optical clearing reagents for fixed tissues have been proposed to increase the tissue penetration depth and enable much deeper imaging.[7–9]

However, the spatial resolution and the fluorescence signal in laser scanning microscopy are frequently degraded by wavefront aberrations caused by refractive-index mismatches in the optical path. These aberrations and their effects have been numerically calculated and experimentally investigated by several authors.[10–13] In many biospecimens, one of the predominant aberrations that deteriorate the quality of an image obtained when observing deep regions of the sample is spherical aberration, which is usually caused by the difference in the refractive index between the sample and the immersion medium.[14] A correction collar is usually built into the body of a high numerical aperture (NA) objective lens to correct some aberrations. However, adjusting the correction collar requires observers to touch the objective lens, which means that the disturbance may affect the accuracy of the adjustment. Similarly, although the alteration of the effective tube length[11] and the refractive index of the immersion medium[10] have been proposed for correcting some spherical aberrations, these techniques are performed statically and are difficult to adjust during observation. On the other hand, some adaptive optics techniques have been previously proposed. Electrically controllable spatial light modulators (SLMs), such as deformable mirror devices or liquid-crystal-on-silicon devices, were shown to reduce not only the spherical aberration but also various other aberrations[15–21] while providing dynamic correction in three-dimensional (3-D) images.[21] For example, with a 40 × /NA1.3 oil immersion objective lens, the imaging depth in water was extended from approximately 3.4 to 46.2 μm by using an SLM in TPLSM.[15] Furthermore, the nonlinear guide-star concept was introduced to the adaptive optics technique using an SLM and succeeded in improving the image quality at deep regions within fixed and *in vivo* biological

*Address all correspondence to: Tomomi Nemoto, E-mail: tn@es.hokudai.ac.jp

samples in TPLSM.[20] However, these refractive SLMs require experimenters to change the basic design of the optical path in a conventional microscope. In these studies, researchers modified the conventional microscope and added a relay optical system in order to incorporate the refractive SLM in the system.[15–21] Such a modification would be difficult to implement for biologists who are not necessarily optics experts.

Liquid-crystal devices have been used in various applications to modulate light waves, e.g., radially polarized beam generators, holographic microscopes, and optical pickups.[22–26] To solve the aforementioned problems, we have developed transmissive liquid crystal devices for the correction of a specific spherical aberration. These devices consist of liquid-crystal cells (LCCs) wherein a layer of liquid crystal molecules is sandwiched by a pair of glass substrates equipped with transparent electrodes. Since the direction of the liquid-crystal molecule exhibiting refractive index anisotropy is electrically controllable, a segmented pattern of the transparent electrode generates a phase distribution that corresponds to a segmented pattern in the wave front of the penetrating light. The phase modulation is controlled by changing the applied voltages.

In our previous study,[27] we numerically calculated spherical aberrations at the pupil of an objective lens when focusing on deep regions of a sample with a homogeneous refractive index. Furthermore, we experimentally confirmed the existence of the calculated spherical aberrations. Moreover, spherical aberrations during deep observations were numerically calculated based on the NA and pupil diameter of the objective lens, and the mentioned liquid crystal devices were designed to correct these spherical aberrations. The optimum design depended on the objective lens. We next evaluated the device by observing beads embedded at various depths in an agarose gel. By inserting the device in front of the objective lens and supplying it with the appropriate voltage to maximize the fluorescence signal of the object, we experimentally demonstrated that the device improved the spatial resolution and the fluorescence signal, which degraded at various regions. In this study, we estimated the axial resolution and evaluated the performance of the device in more detail. Furthermore, we compared experimental and numerical calculation results. Finally, we implemented the device in TPLSM for the observation of a brain slice of a yellow fluorescent protein (YFP) expressing mouse with features of the order of several micrometers. The spatial resolution and the fluorescence signal before and after correction by the device were also estimated. In conclusion, we experimentally demonstrated that the device enhanced the biospecimen's image at various observation depths.

2 Theory and Methods

2.1 *Experimental Setup of the Microscope and Device*

Observations were performed with an upright microscope (Eclipse FN1, Nikon Co.) and a scanner (A1R MP+, Nikon Co.) for excitation light with wavelengths 488 and 950 nm. In this study, the confocal aperture was completely open and the 13-mm-thick device was inserted between a water-immersion objective lens (CFI Apo LWD 25 × W, NA1.1, Nikon Co.) and the microscope revolver. A pulse amplitude modulation controller was used to control the performance of the device [Fig. 1(a)]. Figures 1(b)–1(d) illustrate the principle of the spherical aberration correction by the LCC. Figure 1(b) shows an example of a spherical aberration distribution and Fig. 1(c) shows a schematic of the six-level quantized phase distribution, which corrects the spherical aberration. Figure 1(d) shows the segmented annular electrodes and lead-out electrodes for applying voltage to the liquid-crystal layer to generate the discretized phase distribution in the LCC. The diameter of the outermost peripheral annular electrode was 17.6 mm, which was almost equal to the calculated pupil diameter of the objective lens, according to the manufacturer's information. In this study, we first applied a voltage determined from the numerical calculation. Next, by repeatedly changing the applied voltage slightly, we determined the appropriate voltage required to achieve the maximized fluorescence signal of the object.[27]

After the correction, the discretized phase distribution in the LCC caused a residual aberration, which can be reduced by increasing the number of rings in the phase distribution in the LCC. However, the number of annular electrodes was limited by the production process and could not be further increased. In addition, even if the number of annular electrodes was increased, the corresponding increase in the number of lead-out electrodes would cause a deterioration of the spatial homogeneity and, thus, the optical performance. Therefore, we used numerical calculations to evaluate and optimize the ring number to obtain a maximum effect of correcting the spherical aberration. The numerical calculations were performed based on the Fourier transforming property of lenses. A fast Fourier transform was applied to the phase distribution of the residual aberration on the pupil plane of the objective lens, which resulted in an amplitude distribution on the focus plane. However, the device was not placed in the pupil position of the objective lens during actual implementation. The influence of the displacement of the device from the pupil position along the z-axis is considered in the next section. For an NA1.1 water-immersion objective lens and a sample with a refractive index of 1.38, the amplitude of the induced spherical aberration at a depth of 0.7 mm was calculated as 3600 nm. This value was equal to that of the phase modulation, which can be generated by using three LCCs. The phase distribution quantized in 48 or more levels resulted in a Strehl ratio greater than 0.9 [Fig. 1(e)]. Hence, we used three LCCs to generate a 48-level quantized phase distribution. The LCCs had 31 segmented annular electrodes with linewidths 1.3–0.043 mm. The device achieved a phase modulation of 3600 nm. The phase distribution generated in the device was measured by laser interferometers (Zygo PTI 250, Zygo Corporation) and we confirmed that its form agreed very well with that of the calculated distribution [Fig. 1(f)].

Figure 1(g) shows the transmittance of the LCC. For the wavelength range 800–1100 nm, which was used for excitation in TPLSM, the transmittance was 95% per cell. For the wavelength range 460–600 nm, which was used for fluorescence measurements, the transmittance was 92%–95% per cell. Since we used three LCCs in this study, the transmittance of the device was approximately 88% and 78%–85% in the wavelength ranges 800–1100 and 460–600 nm, respectively.

2.2 *Numerical Calculations Using the Objective Lens System*

The point spread function (PSF) of the 488-nm collimated light beam was numerically calculated (CODEV, Optical Research Associates) assuming that the light was focused through a continuous phase distribution and a 25 × /NA1.1 water-dipping objective lens (JP2011-75982A). The numerical calculation

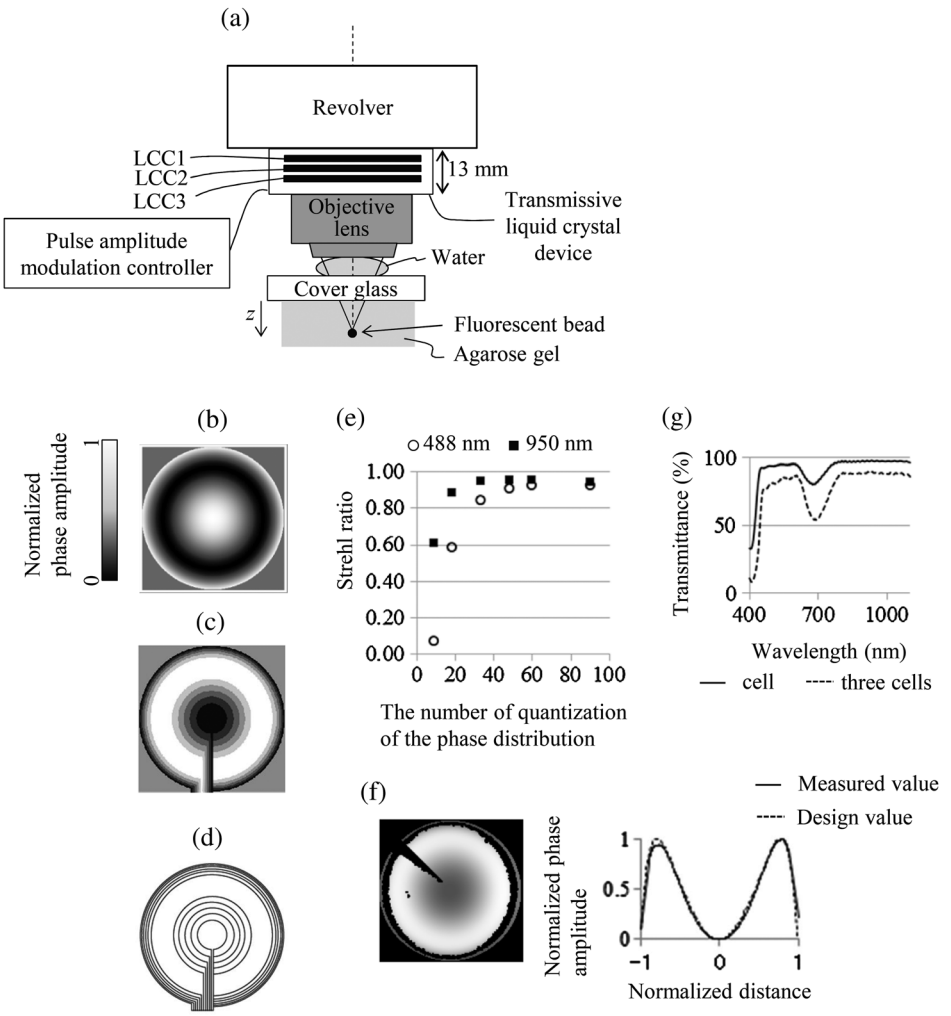

Fig. 1 Experimental setup: (a) configuration of the laser scanning microscope with an adaptive optics device containing liquid crystal cells (LCCs); schematic of (b) spherical aberration and (c) phase distribution of the LCC; (d) schematic of the transparent electrodes in the LCC. (e) Calculated Strehl ratio after correcting spherical aberrations by a quantized phase distribution. (f) The actual phase distribution of the device and the phase profile of the center of the phase distribution. (g) Transmittance of the LCC.

was performed based on the beam propagation method. In this calculation, the continuous phase distribution was placed in a plane perpendicular to the optical axis, 10 mm away from the front of the objective lens along the z-axis (where the device was actually placed in the experiment). To evaluate the effect of the spatially discretized phase distribution of the device with a 48-level quantized phase distribution, the reduction rate of the Strehl ratio was also obtained in the numerical calculation, as mentioned in Sec. 2.1. Therefore, we were able to estimate the influences of both the device's position along the z-axis and the discretization of the phase distribution.

2.3 *Sample Preparation and Analysis*

Fluorescent yellow-green beads with a diameter of 0.2 μm were mixed into agarose gel with a refractive index of 1.38. The refractive index of agarose gel was adjusted using sucrose solutions. The mixture was poured into a glass base dish (cover glass thickness of 0.16–0.19 mm). Under different observation conditions, we observed several beads within the volume of a 20-μm cube located at the center of the field of view. The fluorescence intensity profiles across the intensity center along the x-axis were fitted with a Gaussian function, and the peak intensities and full width at half maximum values along the x-axis (FWHMx values) were obtained for each image. Thus, the average peak intensity and the average FWHMx value of the images were obtained, along with the average intensity profile of those images. Similarly, fluorescence intensity profiles across the intensity center along the z-axis were fitted with a Breit-Wigner-Fano line shape for each image, and the average FWHM value along the z-axis (FWHMz value) and the average intensity profile of those images were obtained.

Previously, 2,2'-thiodiethanol (TDE) solutions were shown to quickly render fixed mouse brain tissues optically transparent.[7,8] TDE-treated fixed mouse brain slices exhibited a higher penetration depth in the visible and the near-infrared regions, and a stronger fluorescence signal was emitted from the deep layers. In this study, we used 51% TDE solutions to clear the 0.95-mm-thick fixed brain slices of YFP expressing mouse (Thy1-YFP-H mouse[28]) and to adjust the refractive index to 1.42. The TDE-treated slices were immersed in a TDE solution of the same concentration in the mount, where the distance

between the cover slip and the slide glass was 1 mm. To estimate the spatial resolution in a fixed brain slice, we utilized dendritic spines about 1 μm in size as a ruler in the cortical layer V neurons. The intensity profiles of a single dendritic spine along the x- and z-axes were fitted with a Gaussian function and a Breit-Wigner-Fano line shape, respectively, to obtain the peak intensities and the FWHM values along the x- and z-axes.

All animal experiments were performed in accordance with the National University Corporation Hokkaido University Regulations on Animal Experimentation and the Guidelines for Proper Conduct of Animal Experiments (Science Council of Japan). The protocol was approved by the Institutional Animal Care and Use Committee of National University Corporation Hokkaido University (Permit No. 10-0119).

3 Results

3.1 *Numerically Calculated Point Spread Function at 488-nm Wavelength*

First, in order to estimate the correction effect of the device, we numerically calculated the PSFs at the surface of the cover glass ($z = 0$ mm) and at depths of 0.3 and 0.6 mm in a sample with a refractive index of 1.38 (Fig. 2). The spatial resolution and the signal of the PSFs degraded in proportion to the depth [Figs. 2(a)–2(d), 2(g), 2(h)]. At a depth of 0.3 mm from the surface of the sample ($z = 0.3$ mm), the peak intensity of the PSF dropped to 13% of the peak intensity at $z = 0$ mm (I_0). Additionally, the FWHMx value degraded to 0.32 μm from 0.22 μm and the FWHMz value to 2.6 μm from 0.77 μm [Figs. 2(k) and 2(l)]. Furthermore, at $z = 0.6$ mm, the peak intensity dropped to 7% I_0 and the FWHMx and FWHMz values degraded to 0.37 and 3.9 μm [Fig. 2(m)], correspondingly. Besides, we confirmed that the spatial resolution and the signal, which degraded as a result of spherical aberrations, improved after correction with the continuous phase distribution placed at the front of the objective lens. [Figs. 2(e), 2(f), 2(i), and 2(j)]. At $z = 0.3$ mm, the peak intensity recovered 93% I_0 [Fig. 2(l)]. On the other hand, we numerically calculated that the peak intensity of the PSF corrected by the 48-level quantized phase distribution was 96% of that corrected by the continuous phase distribution. Therefore, it was assumed that 89% I_0 was recovered after the correction with the quantized phase distribution at the front of the objective lens. Similarly, at $z = 0.6$ mm, the peak intensity recovered by 85% compared to I_0 after the correction by the continuous phase distribution [Fig. 2(m)]. Furthermore, it was numerically calculated that the peak intensity of the PSF corrected by the quantized phase distribution dropped to 90% of that corrected by the continuous phase distribution. Therefore, it was assumed that the peak intensity recovered 77% I_0 after the correction by the quantized phase distribution at the front of the objective lens. On the other hand, at $z = 0.3$ and 0.6 mm, the FWHMz values improved to 0.79 and 0.81 μm, respectively, and the FWHMx values improved to 0.22 μm [Figs. 2(l) and 2(m)]. The FWHM values

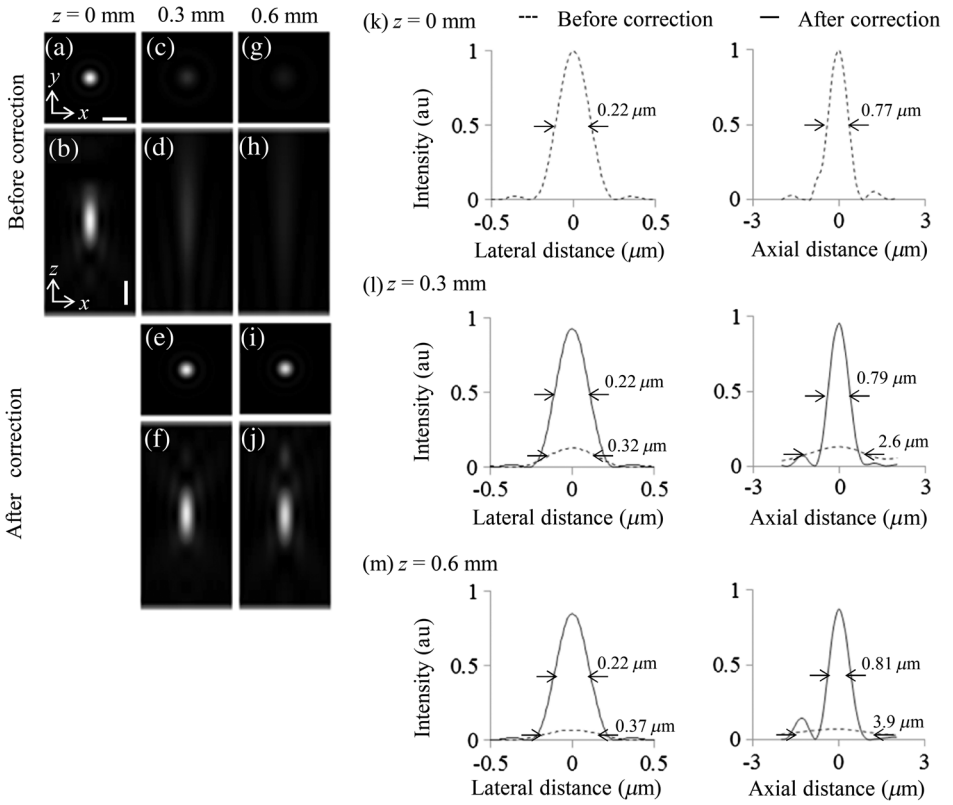

Fig. 2 Numerically calculated point spread functions (PSFs) at a 488-nm wavelength. (a) Lateral and (b) axial images at $z = 0$ mm. Lateral and axial images (c, d) before and (e, f) after correction at $z = 0.3$ mm. Lateral and axial images (g, h) before and (i, j) after correction at $z = 0.6$ mm. (k-m) Intensity profiles across the center of the intensity distribution along the x- and the z-axes at each depth z. The scale bars denote 0.5 μm.

were almost equal to those at $z = 0$ mm, after the correction by the continuous phase distribution.

3.2 *Imaging of the Beads with Single-Photon Excitation Microscopy*

Next, the correction effect of the device was experimentally evaluated by single-photon excitation laser scanning microscopy. In this experiment, fluorescent beads embedded in agarose gel were observed using 488-nm-wavelength laser light to evaluate the fluorescence signal and the FWHM of the image. The correction collar of the objective lens was adjusted beneath the cover glass's surface ($z = 0$ mm) to obtain the best optical performance. At a depth of 0.3 mm from the cover glass surface ($z = 0.3$ mm), the peak intensity of the image dropped to 47% I_0, and the FWHMx value degraded to 0.38 from 0.27 μm. The FWHMz value degraded to 2.8 μm from 1.6 μm [Figs. 3(a)–3(d), 3(k), and 3(l)]. Furthermore, at $z = 0.6$ mm, the peak intensity dropped to 30% I_0. The FWHMx value degraded to 0.42 μm, and the FWHMz value degraded to 5.0 μm [Figs. 3(g), 3(h), and 3(m)]. On the other hand, at $z = 0.3$ mm, the peak intensity recovered by 116% compared to I_0, and the FWHMx value improved to 0.28 μm after correction with the device. Furthermore, the device improved the FWHMz value to 1.2 μm [Figs. 3(e), 3(f), and 3(l)]. Similarly, at $z = 0.6$ mm, the device recovered 78% I_0, and improved the FWHMx value to 0.28 μm. The FWHMz value improved to 1.5 μm after correction by the device [Figs. 3(i), 3(j), and 3(m)]. Namely, at $z = 0.3$ and 0.6 mm, the peak intensities of the corrected images were approximately 2.5 and 2.6 times higher than those of the aberrated images, respectively. Furthermore, the FWHM values were similar to those at $z = 0$ mm after correction with the device.

Next, the correction collar of the objective lens was adjusted to obtain the best performance at $z = 0.7$ mm. At depths smaller than $z = 0.7$ mm, the spatial resolution degraded and the fluorescence signal decreased [Figs. 4(a)–4(d)]. At $z = 0.1$ mm, the peak intensity dropped to 58% of the peak intensity at $z = 0.7$ mm ($I_{0.7}$). Also, the FWHMx and FWHMz values degraded to 0.36 μm from 0.29 μm and to 3.3 μm from 1.8 μm, respectively [Figs. 4(g) and 4(h)]. However, after correction with the device, the peak intensity at $z = 0.1$ mm recovered 94% $I_{0.7}$. Furthermore, the FWHMx value improved to 0.30 μm, and the FWHMz value improved to 1.5 μm [Figs. 4(e), 4(f), and 4(h)]. The correction with the device thus increased the peak intensity by approximately 1.6 times compared to that of the aberrated image. Additionally, the FWHM values improved to the values almost equal to those at $z = 0.7$ mm. From these results, it is evident that the device improved the spatial resolution and the fluorescence signal, and restored the cross-sectioning ability within a depth of ± 0.6 mm.

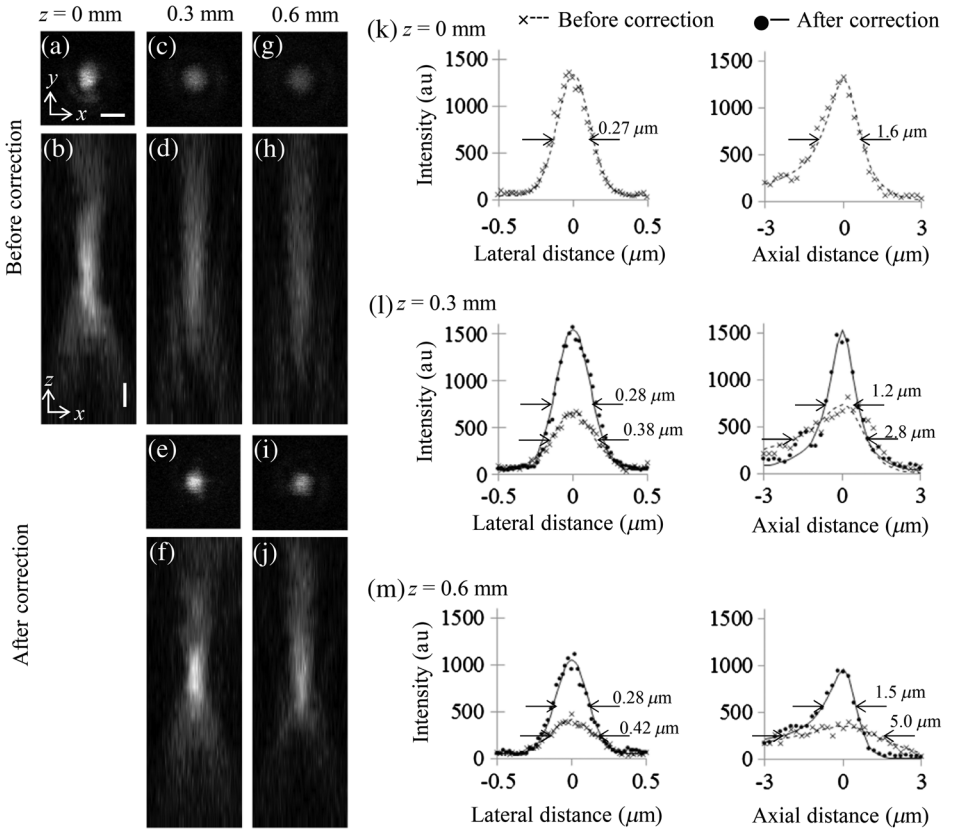

Fig. 3 Images of fluorescent beads in single-photon excitation microscopy illuminated with 488-nm-wavelength laser light. The correction collar of the objective lens was adjusted to obtain the best performance beneath the cover glass surface ($z = 0$ mm). (a) Lateral and (b) axial images at $z = 0$ mm. Lateral and axial images (c, d) before and (e, f) after correction at $z = 0.3$ mm. Lateral and axial images (g, h) before and (i, j) after correction at $z = 0.6$ mm. (k-m) Intensity profiles across the center of the intensity distribution along the x- and the z-axes at each depth z. The data points in (k-m) are the mean values of several beads. The scale bars represent 0.5 μm.

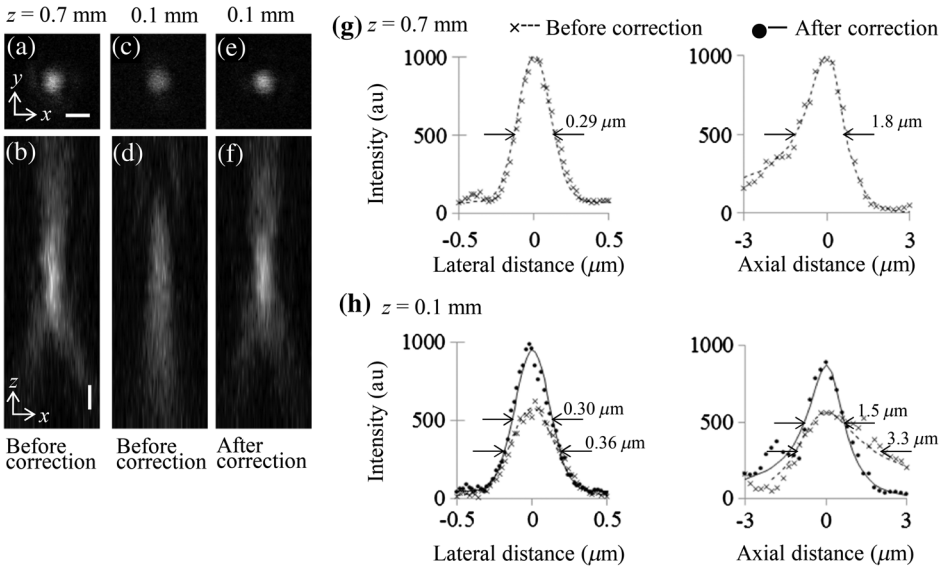

Fig. 4 Images of fluorescent beads in single-photon excitation microscopy illuminated with 488-nm-wavelength laser light. The correction collar of the objective lens was adjusted to obtain the best performance at $z = 0.7$ mm. (a) Lateral and (b) axial images at $z = 0.7$ mm. Lateral and axial images (c, d) before and (e, f) after correction at $z = 0.1$ mm. (g, h) Intensity profiles across the center of the intensity distribution along the x- and the z-axes at each depth z. The data points in (g, h) are the mean values of several beads. The scale bars denote 0.5 μm.

3.3 *Imaging of the Beads with Two-Photon Excitation Microscopy*

In preparation for the implementation of the device to observe a biospecimen using TPLSM, we introduced the device to a TPLSM illuminated by 950-nm-wavelength laser light and observed the fluorescent beads in order to confirm the correction effect of the device. The correction collar of the objective lens was adjusted to obtain the best performance at $z = 0$ mm. As with single-photon excitation microscopy, the spatial resolution and the fluorescence signals of the images degraded in proportion to the depth where the beads were located [Figs. 5(a)–5(d), 5(g), and 5(h)]. At $z = 0.3$ mm, the peak intensity dropped to 67% I_0. Also, the FWHMx and FWHMz values degraded to 0.50 μm from 0.44 μm, and to 3.9 μm from 2.3 μm, respectively [Figs. 5(k) and 5(l)]. Furthermore, at $z = 0.6$ mm, the peak intensity dropped to 45% I_0. The FWHMx value degraded to 0.55 μm, and the FWHMz value degraded to 4.5 μm [Fig. 5(m)]. On the other hand, at $z = 0.3$ and 0.6 mm, the device recovered 115% I_0 and 98% I_0, respectively. The FWHMz values at $z = 0.3$ and 0.6 mm improved to 1.9 and 2.1 μm, correspondingly, and the FWHMx values to 0.44 μm [Figs. 5(e), 5(f), 5(i), 5(j), 5(l), and 5(m)]; namely, the correction by the device increased the peak intensity by approximately 1.7 and 2.2 times, respectively, compared to the aberrated conditions. The FWHM values improved to the value almost equal to those at $z = 0$ mm. At $z = 0.3$ and 0.6 mm, the phase amplitudes generated by the device were 1550 and 3300 nm, respectively. In this way, we succeeded in improving the lateral and axial resolutions. Additionally, the fluorescence signal in deep regions was improved like in the case of single-photon excitation microscopy.

3.4 *Imaging of the Biospecimen with Two-Photon Excitation Microscopy*

Finally, we implemented the device for the observation of the biospecimen described earlier using TPLSM. Figures 6 and 7 show the images of the TDE-treated fixed mouse brain slice. The observation regions were at the surface of the cover glass ($z = 0$ mm) and at depths 0.19, 0.27, and 0.54 mm from the surface. The same areas were observed before and after correcting aberrations. As with the observation of the bead sample, we utilized dendritic spines about 1 μm in size as a ruler to estimate the spatial resolution in the fixed brain slice.

Figure 6 shows the images acquired when the correction collar of the objective lens was adjusted to obtain the best performance at $z = 0$ mm. From the lateral wide-field images at $z = 0.19$ and 0.27 mm, the fluorescence signals improved after correction by the device, as well as with the correction collar [Figs. 6(a)–6(f)]. Furthermore, from the images of the dendritic spines, the device and the correction collar clearly improved the spatial resolution and the fluorescence signal [Figs. 6(g)–6(r)]. Specifically, at $z = 0.19$ mm and a phase amplitude of 2300 nm, the device improved the FWHMx value to 0.48 μm from 0.65 μm and the FWHMz value to 1.4 μm from 3.3 μm. Furthermore, the peak intensity of the image corrected by the device was approximately 1.8 times higher than that of the aberrated image [Fig. 6(s)]. On the other hand, the correction collar improved the FWHMx value to 0.53 μm and the FWHMz value to 1.8 μm. The peak intensity of the image corrected by the correction collar was approximately 2.1 times higher than that of the aberrated image [Fig. 6(s)]. At $z = 0.27$ mm, the device and the correction collar improved the FWHMx value to 0.65 μm from 0.74 μm, they improved the FWHMz value to 1.5 and 1.7 μm from 4.0 μm, respectively, and increased the peak intensity by approximately 2.4 times compared to that of the aberrated condition [Fig. 6(t)]. At $z = 0.27$ mm, the phase amplitude of the device was 2900 nm. In the experiment with the bead sample, the correction by the device with phase amplitude 3300 nm increased the peak intensity 2.2 times compared to that of the aberrated condition (see Sec. 3.3). Accordingly, for the biospecimen, the device showed a similar improvement of the fluorescence signal to that

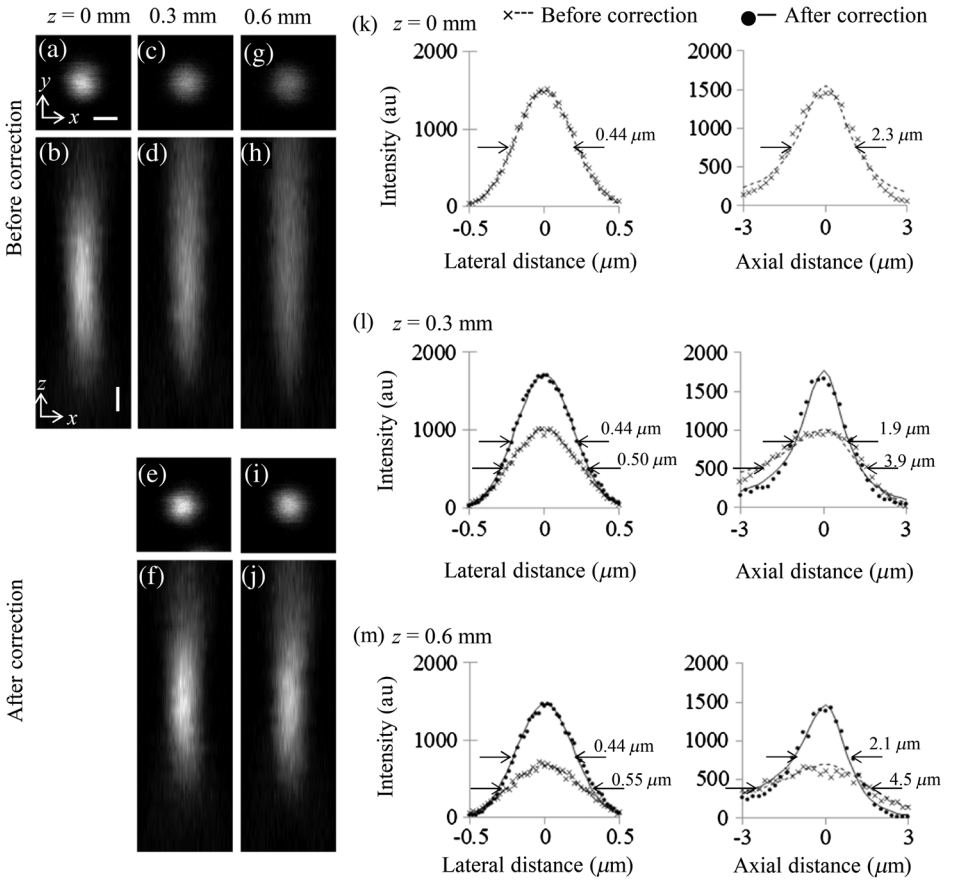

Fig. 5 Images of fluorescent beads in two-photon excitation microscopy illuminated with 950-nm-wavelength laser light. The correction collar of the objective lens was adjusted to obtain the best performance beneath the cover glass surface ($z = 0$ mm). (a) Lateral and (b) axial images at $z = 0$ mm. Lateral and axial images (c, d) before and (e, f) after correction at $z = 0.3$ mm. Lateral and axial images (g, h) before and (i, j) after correction at $z = 0.6$ mm. (k-m) Intensity profiles across the center of the intensity distribution along the x- and the z-axes at each depth z. The data points in (k-m) are the mean values of several beads. The scale bars represent 0.5 μm.

observed for the bead sample. From this result, we confirmed that the device improved the lateral and the axial resolution; additionally, the fluorescence signal degraded in deep regions of the biospecimen, as with the bead sample. Furthermore, the device showed a correction effect similar to that of the correction collar.

Finally, in order to observe a wider range of depth, we adjusted the correction collar to obtain the best performance at a deep region of the biospecimen. In Sec. 3.2, we showed that the device improved the image quality at both shallower and deeper regions than the position in which the best optical performance was obtained. On the other hand, the device improved the image quality at $z = 0$–0.27 mm when the correction collar was adjusted to obtain the best performance at $z = 0$ mm (Fig. 6). Meanwhile, the maximum depth at which the depth-induced spherical aberration was correctable by the correction collar was 0.27 mm. By utilizing this property of the device and the objective lens, the device was expected to improve the image quality at $z = 0$–0.54 mm when the correction collar was adjusted to obtain the best performance at $z = 0.27$ mm. Thus, we observed the biospecimen at depths of 0–0.54 mm. As in Fig. 6, at $z = 0$ and 0.54 mm, the fluorescence signal of the wide-field lateral images improved after correction by the device [Figs. 7(a)–7(d)]. From the images of the dendritic spines, at $z = 0$ mm, the FWHMx and FWHMz values improved to 0.57 μm from 0.66 μm, and to 2.1 μm from 3.2 μm, respectively. Additionally, the peak intensity of the image corrected by the device was approximately 1.5 times higher than that of the aberrated image [Figs. 7(e)–7(h), 7(m)]. Furthermore, at $z = 0.54$ mm, the FWHMx value improved to 0.60 μm from 0.70 μm and the peak intensity of the corrected image was approximately 1.9 times higher than that of the aberrated image. At $z = 0.54$ mm, before correction, the intensity profile along the z-axis extended outside the observation range and the FWHMz value was estimated from the fitting curve. Therefore, the FWHMz value improved to 2.0 μm from 4.5 μm after correction by the device [Figs. 7(i)–7(l), 7(n)]. Thus, by using the device, we succeeded in the acquisition of a high-contrast and high-resolution image of the biospecimen in a wide range of depths, including a depth twice as large as that where depth-induced spherical aberration was correctable by the correction collar.

4 Discussion

We succeeded in improving both the spatial resolution and the fluorescence signal originally degraded by aberrations in agarose gel and in a fixed mouse brain by inserting a transmissive liquid-crystal device between the objective lens and the revolver of the microscope.

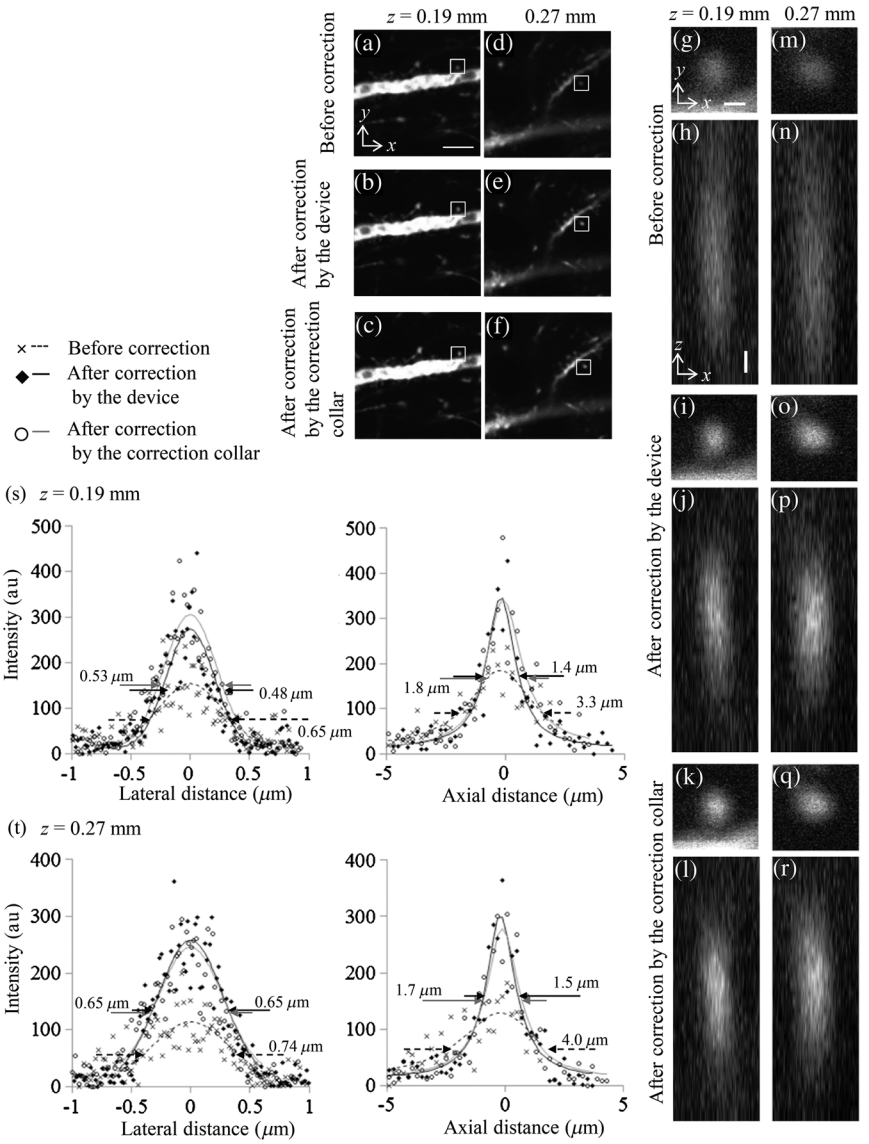

Fig. 6 Images of the biospecimen in two-photon excitation microscopy illuminated with 950-nm-wavelength laser light. Lateral images (a) before and (b) after correction by the device at $z = 0.19$ mm, when the correction collar of the objective lens was adjusted to obtain the best performance beneath the cover glass surface ($z = 0$ mm). (c) Lateral image at $z = 0.19$ mm, when the correction collar of the objective lens was adjusted to obtain the best performance at $z = 0.19$ mm. Lateral images (d) before and (e) after correction by the device at $z = 0.27$ mm, when the correction collar of the objective lens was adjusted to obtain the best performance at $z = 0$ mm. (f) Lateral image at $z = 0.27$ mm, when the correction collar of the objective lens was adjusted to obtain the best performance at $z = 0.27$ mm. The images in (g-r) were obtained in the area indicated by a rectangle in (a-f). (g) Lateral and (h) axial images before and after correction by (i, j) the device and (k, l) the correction collar at $z = 0.19$ mm. Lateral and axial images (m, n) before and after correction by (o, p) the device and (q, r) the correction collar at $z = 0.27$ mm. (s, t) Intensity profiles across the center of the intensity distribution along the x- and the z-axes at each depth z. The scale bars denote 5 μm in (a) and 0.5 μm in (g) and (h).

Figures 6 and 7 show that the correction collar had an effect comparable to or higher than that of our device, although it was difficult to accurately adjust. However, the correction collar would not be able to correct dynamic depth-induced spherical aberrations, because an automatic system involving the rotation of the correction collar without any mechanical vibrations may not be realizable. In the future, an automatic adjustment system with the phase amplitude of our device would enable the dynamic correction of the spherical aberrations of a 3-D image over a wide range of depths. When the correction collar is adjusted to obtain the best performance at deep regions, as shown in Fig. 7, the device would enable visualization in a wider range of depths, including regions where the depth-induced spherical aberration is not correctable by the correction collar. For the sample with a refractive index of 1.42, the device improved the image quality of TPLSM within $z = 0$–0.54 mm. Additionally, for a sample with refractive index 1.52, the device can achieve an optical performance with a Strehl ratio higher than 0.8 at $z = 0$–0.3 mm.

An LCC with aligned liquid-crystal molecules was used to modulate the phase for the linear polarized light in a certain direction. In this study, the device corrected the aberration only

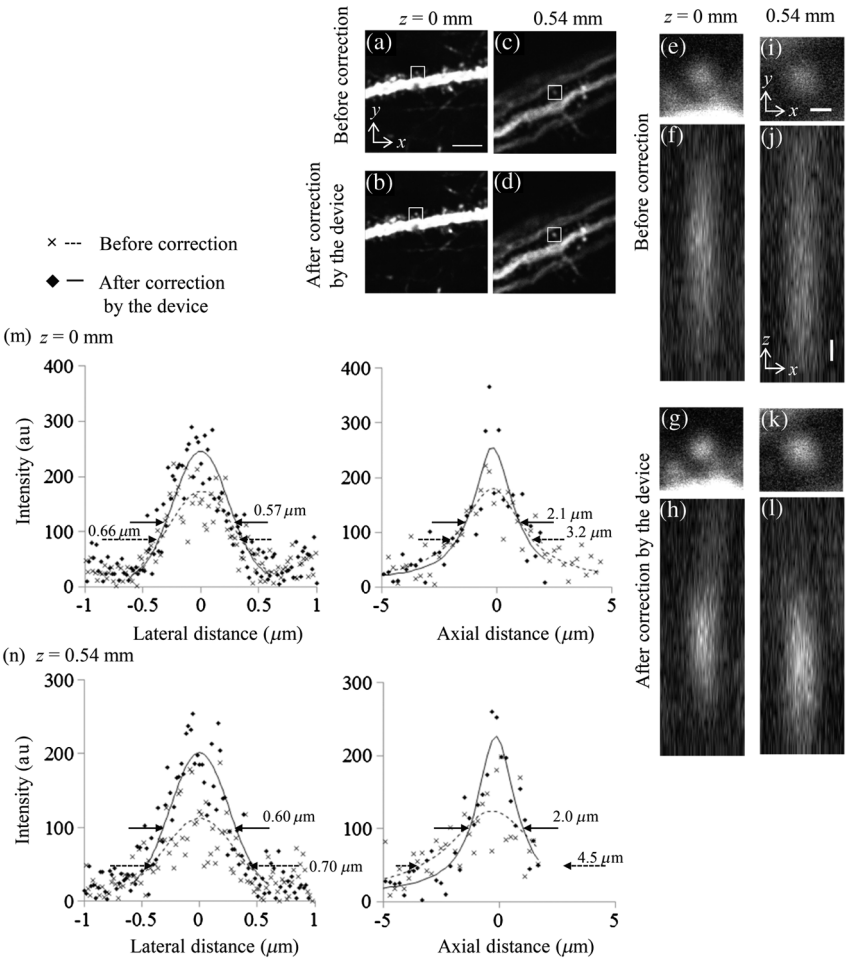

Fig. 7 Images of the biospecimen in two-photon excitation microscopy illuminated with 950-nm-wavelength laser light. The correction collar of the objective lens was adjusted to obtain the best performance at $z = 0.27$ mm. Lateral images (a) before and (b) after correction by the device at $z = 0$ mm. Lateral images (c) before and (d) after correction by the device at $z = 0.54$ mm. The images (e-l) were obtained at the area indicated by the rectangle in (a-d). Lateral and axial images (e, f) before and (g, h) after correction by the device at $z = 0$ mm. Lateral and axial images (i, j) before and (k, l) after correction by the device at $z = 0.54$ mm. (m, n) Intensity profiles across the center of the intensity distribution along the x- and the z-axes at each depth z. The scale bars denote 5 μm in (a) and 0.5 μm in (i) and (j).

for linearly polarized excitation light; the nonpolarized fluorescence signal was not completely modulated. However, since fluorescence detection through the confocal aperture is unnecessary in TPLSM, the aberrated fluorescence signal could be detected by the fluorescent detector; in these measurements no correction was required. In order to integrate the device with confocal laser scanning microscopy, the nonpolarized fluorescence signal also needs to be corrected. It is expected that for confocal laser scanning microscopy, the device will be adapted with two kinds of LCCs, with liquid-crystal molecules aligned in perpendicular directions.

When focusing in deep regions, we found that there was a discrepancy (i.e., a small shift) in the numerical and experimental values of the optimized depths. Therefore, besides other spherical aberration components, additional defocus elements may be included in the phase distribution of the device, which could result in a slightly shifted observation depth after correction by the device. The observation of the same position before and after correction required a fine adjustment of the observation depth after correction. For example, in Fig. 6, the observation depth shifted by 8.0 and 10.3 μm at $z = 0.19$ and 0.27 mm, respectively, after correction by the device. In the future, an automatic adjustment system of the imaging depth according to the amplitude of the phase modulation will be required.

In Figs. 3 and 5, the peak intensity of the corrected images at $z = 0.3$ mm was higher than that at $z = 0$ mm. It is presumed that the device corrects the original coma aberration of the objective lens. The different axial center of the spherical phase distribution and the objective lens induces coma aberration. Therefore, while the device corrects the spherical aberration, the coma aberration of the objective lens may be corrected by the coma phase component generated by the difference in the axial center between the device and the objective lens.

For the 488-nm wavelength, the experimental results qualitatively agreed with the numerically calculated results, while the peak intensity values differed from those of the numerically calculated PSFs (Figs. 2 and 3). Namely, at $z = 0.3$ mm, the numerical and experimental peak intensities and FWHM values of the corrected images were almost equal to those at $z = 0$ mm. On the other hand, at $z = 0.6$ mm, the correction could not

Table 1 The numerically calculated peak intensity of corrected point spread functions (PSFs) compared to that at $z = 0$ mm.

	z (mm)	
Objective lens (×)	0.3 (%)	0.6 (%)
25	89	77
40	94	59
60	84	54

entirely recover the peak intensity, whereas the FWHM values improved to the values almost equal to those at $z = 0$ mm. The correction effect of the device was experimentally confirmed with TPLSM. However, the numerical calculation did not obtain an adequate result because the optical performance of the objective lens system used in the calculation was considerably poor at a 950-nm wavelength. This degradation of the optical performance might be caused by several factors undisclosed by the manufacturer. It is desirable that more information is provided on the specifications of the objective lens.

The degradation of the correction performance at $z =$ 0.6 mm displayed in Figs. 2 and 3 can be explained as follows. The device was theoretically designed to correct a spherical aberration occurring on the pupil of the objective lens; however, the device was not placed exactly at the pupil position on the z-axis. In addition to the 25 × /NA1.1 water-immersion objective lens system, we numerically calculated the correction performance for 40 × /NA1.1 and 60 × /NA1.1 water-immersion objective lens systems (US7889432B and JP4097937B) by the method shown in Secs. 2.1 and 2.2 (Table 1). The numerical calculation revealed that the optical performance after correction lowered proportionally to the focusing depth, especially in the case of the 40× and 60× objective lens systems. It is inferred that the cause of this degradation is the long optical distance between the device and the pupil plane in the high-power objective lens system along the z-axis. In order to improve the performance of the device and to correct such aberrations, more precise numerical calculations for the spherical aberration are required at the real position of the device.

The adaptive optics technique with our device is important for biologists who are not experts in optics and who do not want to change the fundamental optical system of a conventional microscope. Furthermore, the device may also be applicable to conventional confocal laser scanning microscopy or stimulated emission depletion microscopy. The device can be applied to examine various samples, such as live organs. The ultimate goal of our device is the dynamic correction of various aberrations, including asymmetric aberrations such as coma aberration or astigmatism, which are induced by refractive index variations in the sample. In the future, TPLSM with our device is expected to provide a simplified approach to acquiring high-quality images of deep regions in live cells and tissue of fluorescent-protein-expressing transgenic animals.

5 Conclusion

We developed a transmissive liquid-crystal device for correcting spherical aberration. The device was placed in front of the objective lens in a conventional single-photon and a two-photon excitation laser scanning microscope and was shown to improve the spatial resolution and fluorescence signal originally degraded during observation in a wide range of depths. For a 25 × /NA1.1 water-immersion objective lens and a sample with a refractive index of 1.38, the device recovered the spatial resolution and the fluorescence signal of a bead image within a ±0.6-mm depth. Furthermore, we implemented the device in TPLSM for the observation of a fixed mouse brain slice with a refractive index of 1.42. The device improved the spatial resolution and the YFP signal, and restored the cross-sectioning ability within a 0–0.54-mm depth, including the region where the depth-induced spherical aberration was not correctable by a correction collar.

Acknowledgments

We are grateful to Ms. E. Ito and Ms. M. Oguro for their technical assistance. We are also grateful to Dr. Y. Kozawa and Professor S. Sato (Institute of Multidisciplinary Research for Advanced Materials, Tohoku University), and Dr. R. Kawakami, Dr. K. Iijima, Dr. K. Otomo, and Mr. H. Osanai (Research Institute for Electronic Science, Hokkaido University) for their helpful advice. This study was partly supported by JSPS KAKENHI (under Grant Nos. 25-1699, 25560411, 22113005, 22300131, and 26242082) from the Ministry of Education, Culture, Sports, Science, and Technology (MEXT) of Japan; the Nano-Macro Materials, Devices, and System Research Alliance (MEXT); the Network Joint Research Center for Materials and Devices (MEXT); CREST, JST Japan; and Brain/MINDS, AMED, Japan.

References

1. O. Shimomura and F. H. Johnson, "Chemical nature of bioluminescence systems in coelenterates," *Proc. Natl. Acad. Sci. U. S. A.* **72**(4), 1546–1549 (1975).
2. W. Denk, J. H. Strickler, and W. W. Webb, "Two-photon laser scanning fluorescence microscopy," *Science* **248**(4951), 73–76 (1990).
3. R. Kawakami et al., "Visualizing hippocampal neurons with in vivo two-photon microscopy using a 1030 nm picosecond pulse laser," *Sci. Rep.* **3**, 1014 (2013).
4. C. Laperchia et al., "Two-photon microscopy imaging of thy1GFP-M transgenic mice: a novel animal model to investigate brain dendritic cell subsets in vivo," *PLoS One* **8**(2), e56144 (2013).
5. J. T. Trachtenberg et al., "Long-term in vivo imaging of experience-dependent synaptic plasticity in adult cortex," *Nature* **420**(6917), 788–794 (2002).
6. J. Grutzendler, N. Kasthuri, and W. B. Gan, "Long-term dendritic spine stability in the adult cortex," *Nature* **420**(6917), 812–816 (2002).
7. T. Staudt et al., "2, 2'-thiodiethanol: a new water soluble mounting medium for high resolution optical microscopy," *Microsc. Res. Tech.* **70**(1), 1–9 (2007).
8. Y. Aoyagi et al., "A rapid optical clearing protocol using 2, 2-thiodiethanol for microscopic observation of fixed mouse brain," *PLoS ONE* **10**(1), e0116280 (2015).
9. H. Hama et al., "Scale: a chemical approach for fluorescence imaging and reconstruction of transparent mouse brain," *Nat. Neurosci.* **14**(11), 1481–1488 (2011).
10. D. S. Wan, M. Rajadhyaksha, and R. H. Webb, "Analysis of spherical aberration of a water immersion objective: application to specimens with refractive indices 1.33-1.40," *J. Microsc.* **197**(Pt 3), 274–284 (2000).
11. C. J. Sheppard et al., "Influence of spherical aberration on axial imaging of confocal reflection microscopy," *Appl. Opt.* **33**(4), 616–624 (1994).
12. S. F. Gibson and F. Lanni, "Experimental test of an analytical model of aberration in an oil-immersion objective lens used in three-dimensional light microscopy," *J. Opt. Soc. Am. A* **9**(1), 154–166 (1992).
13. M. J. Booth, M. A. A. Neil, and T. Wilson, "Aberration correction for confocal imaging in refractive-index-mismatched media," *J. Microsc.* **192**(Pt 2), 90–98 (1998).

14. M. Schwertner et al., "Measurement of specimen-induced aberrations of biological samples using phase stepping interferometry," *J. Microsc.* **213**(Pt 1), 11–19 (2004).
15. P. Marsh, D. Burns, and J. Girkin, "Practical implementation of adaptive optics in multiphoton microscopy," *Opt. Express* **11**(10), 1123–1130 (2003).
16. L. Sherman et al., "Adaptive correction of depth-induced aberrations in multiphoton scanning microscopy using a deformable mirror," *J. Microsc.* **206**(Pt 1), 65–71 (2002).
17. M. A. Neil et al., "Adaptive aberration correction in a two-photon microscope," *J. Microsc.* **200** (Pt 2), 105–108 (2000).
18. P. Kner et al., "High-resolution wide-field microscopy with adaptive optics for spherical aberration correction and motionless focusing," *J. Microsc.* **237**(2), 136–147 (2010).
19. N. Ji, D. E. Milkie, and E. Betzig, "Adaptive optics via pupil segmentation for high-resolution imaging in biological tissues," *Nat. Methods* **7**(2), 141–147 (2010).
20. R. Aviles-Espinosa et al., "Measurement and correction of in vivo sample aberrations employing a nonlinear guide-star in two-photon excited fluorescence microscopy," *Biomed. Opt. Express* **2**(11), 3135–3149 (2011).
21. X. Tao et al., "Live imaging using adaptive optics with fluorescent protein guide-stars," *Opt. Express* **20**, 15969–15982 (2012).
22. S. Ipponjima et al., "Improvement of lateral resolution and extension of depth of field in two-photon microscopy by a higher-order radially polarized beam," *Microscopy* **63**(1), 23–32 (2014).
23. K. Otomo et al., "Two-photon excitation STED microscopy by utilizing transmissive liquid crystal devices," *Opt. Express* **22**(23), 28215–28221 (2014).
24. Y. Kozawa et al., "Lateral resolution enhancement of laser scanning microscopy by a higher-order radially polarized mode beam," *Opt. Express* **19**(17), 15947–15954 (2011).
25. S. Ohtaki et al., "The applications of a liquid crystal panel for the 15 Gbyte optical disk system," *Jpn. J. Appl. Phys.* **38**, 1744–1749 (1999).
26. G. Brooker et al., "In-line FINCH super resolution digital holographic fluorescence microscopy using a high efficiency transmission liquid crystal GRIN lens," *Opt. Lett.* **38**(24), 5264–5267 (2013).
27. A. Tanabe et al., "Transmissive liquid crystal device correcting the spherical aberrations in laser scanning microscopy," *Proc. SPIE* **9335**, 933502 (2015).
28. G. Fen et al., "Imaging neuronal subsets in transgenic mice expressing multiple spectral variants of GFP," *Neuron* **28**, 41–51 (2000).

Ayano Tanabe is pursuing her PhD degree at Hokkaido University, Japan. She is also involved in development of a liquid-crystal device at Citizen Holdings Co. Ltd. Her current research interests include applications of biomedical imaging. She received her MSc degree in engineering from the University of Electro-Communications.

Terumasa Hibi received his BSc, MSc, and PhD degrees from Nagoya City University. He is an assistant professor at the Research Institute for Electronic Science, Hokkaido University. He has expertise in cell biology and microscopy.

Sari Ipponjima is pursuing her PhD degree at Hokkaido University, Japan. Her current research interests include applications of biomedical imaging. She received her MSc degree in information science from Hokkaido University and her BSc degree in physics from Nara Women's University.

Kenji Matsumoto is an engineer at Citizen Holdings Co. Ltd. His recent interests are optics of microscopy and holography. He received his BS degree in engineering from the University of Electro-Communications.

Masafumi Yokoyama is a chief engineer at Citizen Holdings Co. Ltd. He graduated from Tokyo University of Science in 1987.

Makoto Kurihara graduated from Tokyo University of Science in 1985. He is interested in liquid crystals and their applications.

Nobuyuki Hashimoto received his BSc, MSc, and PhD degrees from Waseda University. After joining Citizen Holdings Co. Ltd., he has been involved in developing applications of liquid-crystal optics in displays, holography, optical data storage, laser printers, telescopes, and bio-imaging. He is a member of SPIE, OSA, and OSJ. He is the president of the holography research group (HODIC) of OSJ.

Tomomi Nemoto received his BSc degree from the University of Tokyo and his MSc and PhD degrees from the Tokyo Institute of Technology. He is a professor at the Research Institute for Electronic Science, Hokkaido University. He has expertise in biological physics and cell physiology.